Longitudinal sampling and aliasing properties in multi-slice helical computed tomography

Patrick J. La Rivière and Xiaochuan Pan

Abstract— **In this work, we investigate longitudinal sampling and aliasing effects in multi-slice helical CT. We demonstrate that longitudinal aliasing can be a significant, complicated, and potentially detrimental effect in multi-slice helical CT reconstructions. Multi-slice helical CT scans are generally undersampled longitudinally for all pitches of clinical interest, and the resulting aliasing effects are spatially variant. As in the single-slice case, aliasing is shown to be negligible at the isocenter for circularly symmetric objects due to a fortuitous aliasing cancellation phenomenon. However, away from the isocenter, aliasing effects can be significant, spatially variant, and highly pitch-dependent. This implies that measures more sophisticated than isocenter slice sensitivity profiles are needed to characterize longitudinal properties of multi-slice helical CT systems adequately. Such measures are particularly important in assessing the question of whether there are preferred pitches in helical CT. Previous analyses have generally focused only on isocenter sampling patterns, and our more global analysis leads to somewhat different conclusions than have been reached before, suggesting that pitches 3, 4, 5, and 6 are favorable, and that half-integer pitches are somewhat suboptimal.**

I. Introduction

With the advent of helical systems and particularly with the advent of the multi-slice helical systems, computed tomography (CT) has become a truly volumetric imaging modality. Image acquisition now involves complicated three-dimensional sampling patterns, and volumetric visualization and analysis techniques have become essential tools for viewing and analyzing the huge amount of reconstructed data produced by each scan.

This move toward volumetric CT imaging brings with it a need for a more complete understanding of the modality's three-dimensional image quality properties. In-plane sampling and resolution properties have been extensively studied in the context of step-and-shoot CT, and most of those properties carry over directly to the helical case. In the longitudinal direction, however, several novel effects of the single-slice helical scan have been identified and studied by Yen *et al* [1, 2]. They showed both analytically and experimentally that single-slice helical CT scans are generally undersampled longitudinally by a factor of at least 2, and that the resulting aliasing effects are highly spatially variant across the field of view due to the peculiarities of the longitudinal sampling engendered by the helical scan. These spatially variant aliasing effects can alter object appearance and contrast across the field view, can make it difficult to set display windows properly, and can generally degrade image quality. Not surprisingly, in single-slice helical CT, the severity of aliasing effects increases monotonically with the helical pitch.

The authors are with the Department of Radiology, The University of Chicago, Chi cago IL 60637 USA.

In this work, we investigate longitudinal sampling and aliasing effects in multi-slice helical CT. While the helical scan is expected to have a similar influence on aliasing as in the single-slice case, the longitudinal interlacing of the multiple detector rows produces very complicated sampling patterns whose effect on aliasing requires careful study. In particular, we expect the severity of aliasing effects (and the transmission of principal frequencies) to vary in complicated, non-monotonic ways as a function of helical pitch. Indeed, we hope to use this study to shed further light on the question of whether there are certain pitches—"preferred pitches"—in multi-slice helical CT that lead to inherently more favorable sampling patterns than do others.

This question has been addressed in many ways and often with a different answer. Hu [3] has argued that pitches 3 and 6 are preferred because the bands of projection-ray dependent complementary samples (discussed below) are centered between the direct samples and thus produce average sampling intervals equivalent to those in single-slice helical CT operating at pitches 1 and 2, respectively. Wang and Vannier [4] performed a "sensitivity analysis" of central detector channel sampling patterns in multi-slice helical CT and reached a nearly opposite conclusion, arguing that pitch 6 is distinctly suboptimal relative to other nearby pitches and that a pitch slightly less than 3 is to be preferred to pitch 3 itself. Both of these sampling analyses are limited in their scope, however, in that they only truly apply to the longitudinal sampling for the central detector channel ($\gamma = 0$), and thus really only predict performance at the system isocenter. Given the extreme variation in longitudinal sampling patterns between central and peripheral detector channels and the spatially variant nature of aliasing effects, we felt it important to develop a more global analysis accounting for the entirety of the longitudinal sampling that arises at each pitch.

II. Methods

A. Theoretical analysis of sampling and aliasing

We begin with a theoretical analysis of longitudinal sampling and aliasing effects in reconstructed multi-slice helical CT volumes. To facilitate comparison with the analysis of single-slice helical CT sampling and aliasing, we adopt and, where necessary, extend the notation of Yen *et al.* [1].

In N-slice helical CT under the multiple parallel fanbeam approximation, we can regard the measured data as samples of a 3D fanbeam sinogram $p_\beta(\gamma, z)$, where β is the projection angle, γ is the angle between the projection ray in question and the central ray of the fanbeam, and z is

the longitudinal position along the object being imaged. In practice, the imaging is performed with detectors of finite longitudinal extent; thus the function being sampled is more appropriately modeled as the convolution of the ideal sinogram and the detector's longitudinal response function, which we denote $a(z)$ (in this work we ignore blurring and sampling effects in the γ coordinate in order to focus on longitudinal effects). Thus we denote by

$$p'_\beta(\gamma, z) = p_\beta(\gamma, z) * a(z)$$

the 3D function whose samples we acquire. Often $a(z)$ is modeled as an ideal rectangular function of width D, where D is the longitudinal detector collimation at the isocenter.

At each of M projection angles $\beta_i = (2\pi i/M)$, $i = 0, \ldots, M-1$, and at each value of γ, the data acquired by the mth detector row in an R-revolution scan at helical pitch P_h comprises samples in z that can be written as

$$s^{(m)}_{\beta_i}(\gamma, z) = p'_{\beta_i}(\gamma, z) \sum_{k=0}^{R-1} \delta\left[z - \left(i\frac{d_{s1}}{M} + kd_{s1} + mD\right)\right], \quad (1)$$

where $d_{s1} = P_h D$. The delta function contains three terms of interest. The first term, $i\frac{d_{s1}}{M}$, reflects the overall longitudinal offset of the sequence at each projection angle; this arises due to the helical nature of the scan. The second term, kd_{s1}, is the actual sampling step, as k is the summation index and d_{s1} is the longitudinal interval between samples at (β_i, γ) and $(\beta_i + 2\pi, \gamma)$. The third term, mD, reflects the overall longitudinal offset of the sequence for the mth detector.

Given these sequences of longitudinal samples at each β_i and γ for each detector row, it is common practice to interpolate a complete sinogram $p^{(\text{int})}_{\beta_i}(\gamma, z)$ at a fixed value of z so that reconstruction can proceed by use of conventional fanbeam reconstruction algorithms. In addition to making use of the *direct* samples of Eq. 1 for interpolation, it is generally advantageous to exploit the redundancy of fanbeam data acquired over 2π to augment these samples with the *complementary* samples $s^{(m)}_{\beta_i+\pi+2\gamma}(-\gamma, z)$ that correspond geometrically to the same projection ray as $s^{(m)}_{\beta_i}(\gamma, z)$, only shifted longitudinally by $\left(\frac{\pi+2\gamma}{2\pi}\right) d_{s1}$. The most straightforward interpolation approach, 180MLI, makes use of linear interpolation among these direct and complementary samples, and it can be expressed as

$$\begin{aligned} p^{(\text{int})}_{\beta_i}(\gamma, z) &= \sum_{m=0}^{N-1} \left[s^{(m)}_{\beta_i}(\gamma, z) *_z h^{(m)}_d(\gamma, z) \right. \\ &+ \left. s^{(m)}_{\beta_i+\pi+2\gamma}(-\gamma, z) *_z h^{(m)}_c(\gamma, z) \right] \quad (2) \end{aligned}$$

where $*_z$ denotes a 1D convolution in the variable z, and $h^{(m)}_d(\gamma, z)$ and $h^{(m)}_c(\gamma, z)$ are the linear interpolation kernels applied to the direct and complementary samples, respectively, of the mth detector row. In the z variable, these kernels have the form of an asymmetric triangle function. The half-widths of these asymmetric triangles can be computed empirically from the sampling patterns that arise when the direct and complementary samples for all rows are interlaced appropriately at each γ.

Given a stationary fanbeam sinogram $p^{(\text{int})}_{\beta_i}(\gamma, z)$, the penultimate step of the reconstruction process is to filter it in the γ direction,

$$q_{\beta_i}(\gamma, z) = \left[D_0 \cos(\gamma) p^{(\text{int})}_{\beta_i}(\gamma, z)\right] *_\gamma g(\gamma), \quad (3)$$

where D_0 is the fanbeam focal length, and $g(\gamma)$ is the fanbeam reconstruction filter. Reconstruction of an image $f(r, \phi, z)$, expressed here in polar coordinates, is then achieved by use of

$$f(r, \phi, z) \approx \Delta\beta \sum_{i=0}^{M-1} \frac{1}{L^2(r, \phi, \beta_i)} q_{\beta_i}(\gamma', z), \quad (4)$$

where $L(r, \phi, \beta_i)$ and γ' are known functions of r, ϕ, and β_i defined in [1, 5].

Equation 4 can be viewed as an expression for a continuous 3D volume $f(r, \phi, z)$ reconstructed from the measured, sampled data $s^{(m)}_{\beta_i}(\gamma, z)$. We are interested in the effect that the longitudinal sampling during the measurement process has on the longitudinal properties of the reconstructed volume. Thus we regard $f(r, \phi, z)$, for fixed (r, ϕ) as a continuous 1D function of z, which we denote $f_{(r,\phi)}(z)$, and will examine the spectrum of the resulting profiles. In practice, of course, we do not reconstruct volumes that are continuous in the z coordinate, but rather that comprise a finite set of slices spaced by a reconstruction interval d_{s2}. However, because we are interested in the effect of the acquisition sampling, we can safely disregard this resampling step.

Computing the Fourier transform with respect to z of Eq. 2, as in [1], yields

$$\begin{aligned} \mathcal{F}_z\left\{f_{(r,\phi)}(z)\right\} = \Delta\beta D_0 R \sum_{i=0}^{M-1} \left\{ \frac{1}{L^2(r, \phi, \beta_i)} \left[\cos(\gamma)\right.\right. \\ \left.\left. \times \sum_{k=-\infty}^{\infty} P'_{\beta_i}\left(\gamma, f_z - \frac{k}{d_{s1}}\right) e^{-j2\pi i \frac{k}{M}} H'_k(\gamma, f_z)\right] *_\gamma g(\gamma)\right\}\Bigg|_{\gamma'} \quad (5) \end{aligned}$$

where

$$\begin{aligned} H'_k(\gamma, f_z) &= \sum_{m=0}^{N-1} e^{-j2\pi k \frac{m}{P_h}} \left[H^{(m)}_d(\gamma, f_z)\right. \\ &+ \left. H^{(m)}_c(-\gamma, f_z) e^{-jk(\pi+2\gamma)}\right], \quad (6) \end{aligned}$$

and where $H^{(m)}_d(\gamma, f_z)$, $H^{(m)}_c(\gamma, f_z)$, and $P'_{\beta_i}(\gamma, f_z)$ are the Fourier transforms with respect to z of $h^{(m)}_d(\gamma, z)$ and $h^{(m)}_c(\gamma, z)$, and $p'_{\beta_i}(\gamma, z)$, respectively.

Equation 5 allows us to draw some conclusions about potential aliasing effects. It can be argued that the helical CT data is at least approximately bandlimited longitudinally

by the first zero of the rectangular detector response function, which occurs at $f_z = 1/D$ [1]. Satisfying the Nyquist sampling condition would thus require a sampling interval $d_{s1} = D/2$. From Eq. 5, it can be seen that the fundamental sampling interval, which determines the spacing of the spectral replications $P'_{\beta_i}\left(\gamma, f_z - \frac{k}{d_{s1}}\right)$ is $d_{s1} = P_h D$, and thus the Nyquist condition is not satisfied for reasonable values of P_h. In general, then, we might expect substantial aliasing effects characteristic of sampling at interval $P_h D$. However, the phase factors in Eqs. 5 and 6 can lead to partial or complete cancellation of aliasing in some circumstances.

The first such case arises when the helical pitch P_h is an integer less than or equal to the number of detector rows N. In this case, the $H^{(m)}(\gamma, f_z)$ are all of the form $w_m H(\gamma, f_z)$, where the w_m are normalization weights chosen so that the w_m for detector rows that follow the same trajectories sum to 1. Given this, it is possible to show that the only remaining m dependence in Eq. 6 is contained in a term of the form:

$$\sum_{m=0}^{P_h-1} e^{-j2\pi k \frac{m}{P_h}} = \begin{cases} P_h, & \text{for } k = 0, \pm P_h, \pm 2P_h, \ldots \\ 0, & \text{otherwise} \end{cases}$$

In this case, it is possible to replace all the k in Eq. 5 by $P_h k$, and thus the effective sampling interval becomes $d_{s1}/P_h = D$. This interval still does not satisfy the Nyquist condition, but the nature and severity of the aliasing effects will be substantially altered relative to the general, non-integer pitch case.

The second situation in which we might expect outright aliasing cancellation is at the system isocenter when imaging circularly symmetric objects, a phenomenon demonstrated by Yen *et al.* for single-slice helical CT. In this situation, it is possible to manipulate Eq. 5 to isolate a factor of the form

$$\sum_{i=0}^{M-1} e^{-j2\pi i \frac{k}{M}} = \begin{cases} M, & \text{for } k = 0, \pm M, \pm 2M, \ldots \\ 0, & \text{otherwise,} \end{cases} \quad (7)$$

and thus the effective isocenter sampling interval becomes d_{s1}/M, a reduction by the number of projection angles per revolution!

B. Numerical evaluation of analytic results

B.1 Spatial distribution of aliasing effects

In order to study the spatial distribution of aliasing effects, we evaluated Eq. 5 for a circularly symmetric, cylindrical object with radius R_c and with sinusoidal longitudinal variation of frequency f_0. That is, we assumed

$$p_\beta(\gamma, z) = p_\gamma(\gamma) \cos(2\pi f_0 z),$$

where

$$p_\gamma(\gamma) = \begin{cases} \sqrt{R_c^2 - D_0^2 \sin^2(\gamma)}, & \gamma \le \sin^{-1}(R_c/D_0) \\ 0, & \gamma > \sin^{-1}(R_c/D_0) \end{cases}.$$

Thus

$$P_\beta(\gamma, f_z) = p_\gamma(\gamma) \left\{ \frac{1}{2} \left[\delta(f_z - f_0) + \delta(f_z + f_0) \right] \right\}.$$

This object is similar to the cylindrical, square-wave phantom employed by Yen *et al.* [1], and it allows us to isolate and quantify aliasing effects easily. An ideal reconstruction would have energy only at the frequencies $f_z = \pm f_0$. However, due to aliasing effects we actually expect energy at $f_z = \pm f_0 + \frac{k}{d_{s1}}$, for $k \in \mathbb{Z}$. For one such frequency of interest f_z we evaluate the factor in square brackets in Eq. 5 by computing the sum over the appropriate values of k (in most cases, only one k contributes to each f_z of interest). We evaluate $H^{(m)}(\gamma, f_z)$ by computing the asymmetric triangles $h^{(m)}(\gamma, z)$ on a discrete (γ, z) grid, heavily zero-padding in z, and then taking a discrete Fourier transform to obtain estimates of $H^{(m)}(\gamma, f_z)$ on a discrete (γ, f_z) grid. The quantity in square brackets can be expressed as a 2D, complex-valued array having dimensions of a sinogram, and thus $\mathcal{F}_z\left\{f_{(r,\phi)}(z)\right\}$ can be computed on a Cartesian grid simply by applying a fanbeam filtered backprojection routine to the real and imaginary components of this sinogram-like quantity. The magnitude of the resulting complex-valued image gives the magnitude of the longitudinal spectrum at frequency f_z at each transverse point in the reconstructed volume.

We evaluated such images for a 4-row system at a number of pitches, using a cylindrical phantom of radius 230 mm and fundamental frequency $f_0 = 1/3.175$ mm^{-1}. We modeled the detector response as rectangular, with longitudinal collimation 2.5 mm at the isocenter. We used 128 projection angles and 128 equiangular projection rays, spaced by 4 mm at the isocenter, and a focal length of 540 mm. Typical results are given in Sec. III-A.

B.2 Contrast to aliased noise as a function of pitch

In addition to examining the spatial distribution of aliasing effects, we also sought to quantify the severity of aliasing effects as a function of helical pitch, in an effort to shed some light on the issue of whether there are preferred pitches in multi-slice helical CT. To do so, we adopted the point of view of Park *et al.* [6], in which aliasing is regarded as structured, signal-dependent noise that can interfere with the detection of a signal. We then computed a *contrast-to-aliased-noise ratio* (CN_aR) for reconstructions of the object discussed in Sec. II-B, using the geometry discussed there, for pitches ranging from 1.0 to 8.0 in increments of 0.1. Yen *et al.* also used a CN_aR figure of merit in their consideration of single-slice helical CT [2]. However, in that case, the main frequency produces only a single low-frequency aliased peak of interest, and so they define CN_aR for a single longitudinal profile simply in terms of the amplitudes of the reconstructed main and aliased spectral peaks. In the multi-slice case, there will, in general, be numerous aliased peaks at low frequencies. We are also interested in a more global measure of aliasing content in

an entire reconstructed volume. Thus we define

$$CN_aR(P_h) = 20 * \log_{10} \frac{\sqrt{\sum_i \sum_j |F_{P_h}(x_i, y_j, f_0)|^2}}{\sqrt{\sum_{f_a} \sum_i \sum_j |F_{P_h}(x_i, y_j, f_a)|^2}},$$

where $F_{P_h}(x_i, y_j f_z)$ is the spectral magnitude image for frequency f_z on a Cartesian grid. The i and j sums run over pixels less of distance less than R_c from the image center and the f_a sum runs over aliased frequencies between 0 and $2/D$. Note that CN_aR is expressed in decibels.

III. Results

A. Spatial variance of aliasing effects

Figure 1 depicts the magnitude $|F_{P_h}(x_i, y_j, f_z)|$ for $i = 64, \ldots 127$, $j = 64$, and three values of f_z: $f_z = f_0$, $f_z = f_{a1} = \left(-f_0 + \frac{1}{D}\right)$, and $f_z = f_{a2} = \left(f_0 + \frac{1}{D}\right)$. These are the only three values of $f_z \in \left[0, \frac{2}{D}\right)$ for which the spectral magnitude is non-negligible. This fact alone confirms the finding in Sec. II-A that the effective sampling interval is D and not DP_h for integer pitches less than or equal N. Otherwise, we would have expected to find non-negligible spectral magnitude at, for instance, $f_z = \left(-f_0 + \frac{1}{3D}\right)$. The figure itself confirms the spatially variant nature of the aliasing effects, which increase in magnitude from zero at the isocenter to a maximum near the periphery of the phantom.

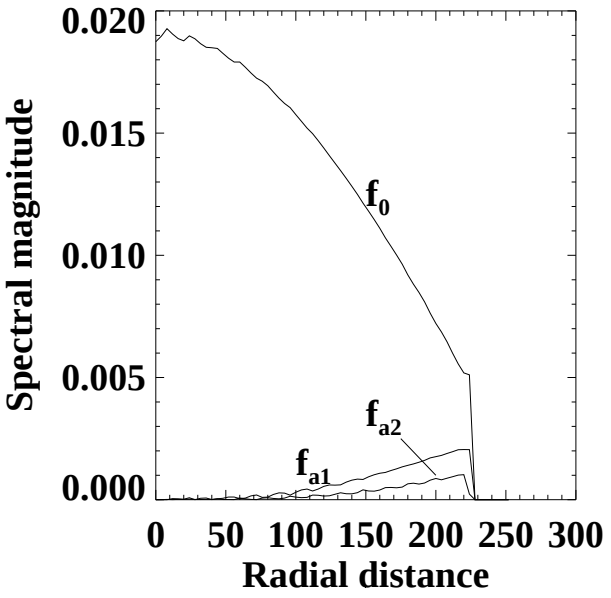

Fig. 1. Spatial dependence of longitudinal spectral magnitude for three frequencies of interest along a line from the isocenter to the edge of the phantom.

B. Contrast to aliased noise as a function of pitch

Figure 2 plots the calculated CN_aR versus helical pitch; higher values of CN_aR are better. As expected, the curve

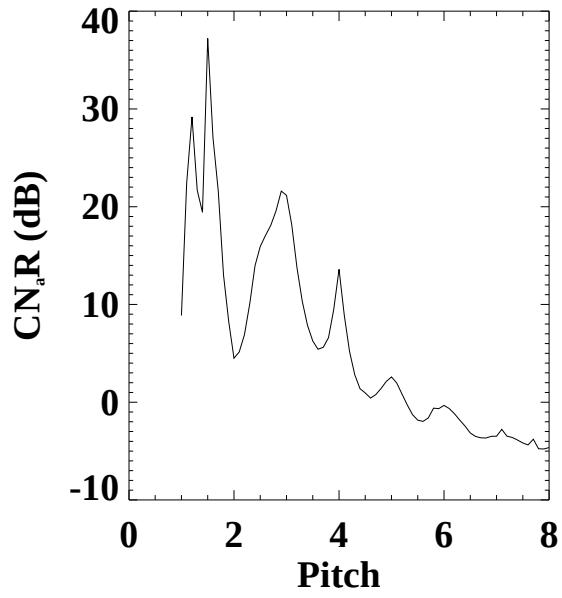

Fig. 2. $CN_a\,R$, in decibels, versus helical pitch for a four-slice scanner with longitudinal collimation width 2.5 mm at the isocenter imaging an object with sinusoidal longitudinal variation of frequency $f_0 = 1/3.175$ mm^{-1}. Higher values of $CN_a\,R$ are better.

is far from monotonic. Local maxima are evident around pitches 3, 4, 5, and 6. Some complicated variation is evident between pitches 1 and 2, with pitch 2 being a clear minimum in the curve. Other minima occur at half-integer pitches.

An intuitive explanation of these results can be obtained by considering the longitudinal sampling patterns that arise at various pitches and at various values of γ. For example, at pitch 3, the direct samples of the four detector rows interlace to form a uniform sampling pattern with interval D. At $\gamma = 0$, the complementary data reside midway between these direct samples, and thus provides effective sampling interval of $D/2$, which allows relatively narrow interpolation kernels to be applied. At larger values of γ, the complementary data approaches but do not, in general, cross over the direct samples, and thus do continue to provide some measure of stable aliasing suppression.

Perhaps the most surprising aspect of Fig. 2 is the peak at pitch 4, which is generally considered a poor choice because of its unfavorable isocenter SSP performance. As at pitch 3, the direct samples of the four detector rows interlace to form a uniform sampling pattern with interval D. However, now at $\gamma = 0$, the complementary data are coincident with these direct samples, and relatively broad interpolation kernels must be applied; this explains the poor isocenter SSP performance. However, for larger values of γ, which contribute most to areas of the reconstructed volume where aliasing is likely to be problematic, the complementary data reside nearly midway between the direct samples and thus provide a measure of aliasing suppression where it is needed most.

IV. Discussion and conclusions

We have demonstrated that longitudinal aliasing can be a significant, complicated, and potentially detrimental effect in multi-slice helical CT reconstructions. Multi-slice helical CT scans are generally undersampled for all pitches of clinical interest, and the resulting aliasing effects are spatially variant.

As in the single-slice case, aliasing is negligible at the isocenter for circularly symmetric objects due to a fortuitous aliasing cancellation phenomenon. The effective oversampling at the isocenter of such objects explains why it is even possible to obtain reasonable looking slice sensitivity profiles (SSP) and longitudinal modulation transfer functions of an ostensibly undersampled system: these measurements are always performed at the isocenter by use of a circularly symmetric phantom. However, this phenomenon in no way licenses the use of these measures to characterize longitudinal resolution properties of multi-slice helical CT systems. Away from the isocenter, aliasing effects can be significant, spatially variant, and highly pitch dependent. More sophisticated measures of longitudinal properties are needed to characterize multi-slice helical CT systems adequately.

Such measures are particularly important in assessing the question of whether there are preferred pitches in helical CT. Previous analyses have generally focused only on isocenter sampling patterns, and thus predict isocenter SSP performance, but neglect aliasing effects away from the isocenter. Our more global analysis suggests that the much maligned pitch 4, despite its poor isocenter SSP performance, actually yields a very favorable global CN_aR because of favorably uniform longitudinal sampling for its outer detector channels. The analysis did confirm the advantages of pitches 3 and 6, and also suggested that pitch 5 would be favorable. Half-integer pitches appeared to be poor performers by this measure.

The analysis performed above implicitly blends sampling and interpolation effects. In this work, we examined the use of straightforward linear interpolation. In practice, straightforward linear interpolation is rarely used because frequent "changeovers" in the pairs of detector rows contributing to a given slice tend to produce artifacts in reconstructed images. In general, either attention is restricted to pitches where linear or quasi-linear approaches can be applied safely [3] or broader, adaptive z-filtering interpolation approaches are employed [7, 8]. We do not expect that the use of a different interpolation approach would fundamentally alter the conclusions of this study. The presence of longitudinal aliasing effects and their spatial distribution are effectively inherent properties of the helical scan geometry. Altering the interpolation approach might alter the transmission of principal, unaliased frequencies somewhat, but would not be expected to affect aliasing effects profoundly. Nonetheless, we do intend to extend our analysis to these alternative approaches, as their longitudinal properties have only been characterized through use of SSP measurements, whose limitations should be evident from the preceding discussions.

One effect that was not considered in great detail in this summary is the small cone angle that arises in multi-slice helical CT. This cone angle has generally been ignored in deriving reconstruction algorithms and sampling analyses by making the multiple parallel fanbeam assumption made here, *i.e.* by assuming that the multi-row data comprises multiple, parallel transverse projections of the object, not multiple, differently oblique ones. This approximation is regarded as reasonably sound for systems of 4 or fewer rows, although we have shown elsewhere that the small cone beam angle does influence longitudinal sampling and aliasing properties by introducing inconsistencies among the data measured by the different detector rows [9]. We felt justified in ignoring the effect in the present summary because we felt that we could contribute a novel, thorough analysis of sampling in multi-slice helical CT under the approximation that has been the foundation of all previous analyses. The development of a more complete analysis that does account for the cone angle effect is the subject of ongoing work.

References

[1] S. Y. Yen, C. H. Yan, G. D. Rubin, and S. Napel, "Longitudinal sampling and aliasing in spiral CT," *IEEE Trans. Med. Imag.*, vol. 18, pp. 43–58, 1999.

[2] S. Y. Yen, G. D. Rubin, and S. Napel, "Spatially varying longitudinal aliasing and resolution in spiral computed tomography," *Med. Phys.*, vol. 26, pp. 2617–2625, 1999.

[3] H. Hu, "Multi-slice helical CT," *Med. Phys.*, vol. 26, pp. 5–18, 1999.

[4] G. Wang and M. W. Vannier, "The effect of pitch in multislice spiral/helical CT," *Med. Phys.*, vol. 26, pp. 2648–2653, 1999.

[5] A. Rosenfeld and A. C. Kak, *Digital Picture Processing*, Academic Press, New York, 1982.

[6] S. K. Park and R. Hazra, "Image restoration versus aliased noise enhancement," in *Proc. SPIE*, 1994, vol. 2239, pp. 52–62.

[7] K. Taguchi and H. Aradate, "Algorithm for image reconstruction in multi-slice helical CT," *Med. Phys.*, vol. 25, pp. 550–560, 1998.

[8] S. Schaller, T. Flohr, K. Klingenbeck, J. Krause, T. Fuchs, and W. Kalendar, "Spiral interpolation algorithms for multi-slice spiral CT part I: Theory," *IEEE Trans. Med. Imag.*, vol. 19, pp. 822–834, 2000.

[9] P. J. La Rivière and X. Pan, "Longitudinal sampling and aliasing in multi-slice helical CT," in *Proc. 2000 IEEE Nucl. Sci. Symp. and Med. Imag. Conf.*, 2000, To appear.